Supplement of Earth Syst. Dynam., 16, 1779–1808, 2025 https://doi.org/10.5194/esd-16-1779-2025-supplement © Author(s) 2025. CC BY 4.0 License.





Supplement of

A new biogeochemical modelling framework (FLaMe-v1.0) for lake methane emissions on the regional scale: development and application to the European domain

Manon Maisonnier et al.

Correspondence to: Maoyuan Feng (maoyuan.feng@ulb.be)

The copyright of individual parts of the supplement might differ from the article licence.

S1. Overview of the lake physical model–CLSM

The Canadian Small Lake Model (CSLM) is a 1D thermal model designed to simulate the water temperature profiles (T) and relevant variables (e.g., mixing depths (h_{mix}) and ice cover dynamics) (MacKay, 2012; MacKay *et al.*, 2017). Here, we introduce the CSLM briefly, and the detailed mathematical descriptions, numerical schemes, and parameterizations of CSLM can be found in MacKay (2012). The CSLM computes the profiles of water temperature and light penetration, mixing depths, and ice dynamics, which set the basis for the simulation of the biogeochemical modules (organic carbon, oxygen, and methane) implemented in the FLaMe model. CSLM adopts a turbulent mixing parameterization, which relies on a depth-integrated turbulent kinetic energy (TKE) approach (MacKay 2012).

The meteorological variables required to force CSLM include shortwave and longwave radiation, precipitation, atmospheric temperature and pressure, near-surface wind speed, and specific humidity. The general heat transfer process (without turbulence and mixing layer) within the lake is described as follows:

$$\frac{\partial T}{\partial t} = -\frac{1}{\rho c_w} \frac{\partial F}{\partial z} - \frac{1}{\rho c_w} \frac{\partial Q}{\partial z}$$
 (S1)

$$F(z) = -K \frac{\partial T}{\partial z}$$
 (S2)

where T is the temperature of the lake at a given depth z and time t, ρ is the water density, c_w is the water specific heat capacity, F is the heat flux resulting from thermal conduction, K is the water thermal conductivity, and Q is the radiative energy flux, which decreases with depth according to Beer's law. This equation is solved numerically using an explicit forward finite difference scheme in time.

To constrain the temperature at the lake surface, the surface energy balance is described as follows:

43
$$\frac{\partial T_0}{\partial t} = -\frac{1}{\delta_0 \rho c_w} [F_0 - (L^* - H_S - H_E) + Q_0 - Q^*]$$
 (S3)

where T_{θ} is the surface layer temperature, also called "skin" temperature, δ_{θ} is the thickness of the skin, F_{θ} and Q_{θ} are thermal and solar energy flux, respectively, transmitted from the skin to the water column. L^* is the surface net longwave radiation, H_S and H_E are the turbulent sensible and latent heat fluxes into the atmosphere, respectively. Q^* is the surface net solar radiation that penetrates the lake water. This description allows ice formation when $T_{\theta} < 0$ °C. The details of the parameterization of this equation can be found in MacKay (2012).

If we consider the turbulence and resultant mixed layer, the depth-integrated turbulent kinetic energy (TKE) approach can be described briefly as follows. Driven by wind, the upper portion of the lake water is mixed by TKE, leading to a surface mixed layer. Within this mixed layer, the TKE is dynamically calculated as follows:

$$\frac{d}{dt}(uh_{mix}) = u_*^2 \tag{S4}$$

$$\frac{d}{dt}\left(\frac{1}{2}h_{mix}E_s\right) = \frac{h_{mix}}{2}\frac{dE_s}{dt} + \frac{E_s}{2}\frac{dh_{mix}}{dt} \tag{S5}$$

where u is the mean horizontal velocity within the mixed layer, h_{mix} is the depth at the bottom of the mixed layer, u^* is the surface friction velocity induced by near-surface wind, and E_S is the average TKE per unit mass in the mixed layer. Equations (S4) and (S5) specifies the momentum balance and the depth-integrated TKE budget, respectively, within the mixed layer.

The surface friction velocity u^* is estimated from the atmospheric near-surface wind speed U_a as

61 follows:

66

67

68

69

70

71

$$u_* = \frac{C_D \rho_a^{1/2}}{\rho} U_a \tag{S6}$$

- where C_D is the drag coefficient and ρ_a is the air density.
- To constrain E_S in Eq. (S5), the energy budget within the mixed layer is described as follows:

$$\frac{d}{dt}\left(\frac{1}{2}h_{mix}E_{s}\right) = F_{q} - F_{d} + F_{s} - F_{p} - F_{L} \tag{S7}$$

where F_q is the mechanical energy caused by wind and buoyancy effects, F_s is the shear production flux caused by the stabilization effect of the thermocline at the bottom of the mixed layer, F_d is the energy dissipation flux within the mixed layer, F_i is the transport of TKE to the thermocline, F_L is the TKE leakage flux caused by internal wave propagation away from the mixed layer, and F_p is the change in potential energy flux caused by the change in thermocline depth. To close the system of equations, the energy balance within the mixed layer can be separated into two components:

$$\frac{h_{mix}}{2} \frac{dE_s}{dt} = F_q - F_d - F_i \tag{S8}$$

$$\frac{E_s}{2} \frac{dh_{mix}}{dt} = F_i + F_s - F_p - F_L \tag{S9}$$

These two equations can be used to solve the dynamics of E_S and h_{mix} , respectively, which rely only on the model parameters and meteorological forcings (see details in MacKay 2012).

S2. Methods for estimating the threshold depth for the split of diffusion and ebullition

Following Langenegger *et al.* (2019), we assumed an exponentially decreasing function to describe the decay of methane production rate versus sediment depth, and adopted a threshold depth $z_{\rm eb,min}$ to split the CH₄ production into diffusive and ebullitive transport pathway. Driven by the CH₄ production, the CH₄ concentration increases as the sediment depth increases. Therefore, at a certain threshold sediment depth, the CH₄ concentration may exceed its solubility limit and bubbles may start forming (Fig. 3 in the main text). This threshold depth, $z_{\rm eb,min}$, is the depth at which the sum of partial pressure of CH₄ and N₂ exceed the sum of the hydrostatic and atmospheric pressure. Following Langenegger *et al.*, (2019), $z_{\rm eb,min}$ is determined by the following equation:

85
$$\underbrace{K_{H,CH_4}[CH_4]_s + K_{H,N_2}[N_2]_s}_{\text{total dissolved gas pressure}} = \underbrace{\rho g h}_{\text{hydrostatic pressure}} + \underbrace{P_{\text{atm}}}_{\text{atmosphere pressure}} - \underbrace{P_{H_2O}}_{\text{water vapor saturation pressure}}$$
(S10)

where $K_{H,CH4}$ and $K_{H,N2}$ are Henry's constants of CH₄ and N₂, respectively. The dissolved gas pressure of CH₄ ([CH₄]_s) is determined by the CH₄ production rate and its exponentially decreasing distribution versus sediment depth z_s , while the dissolved gas pressure of N₂ ([N₂]_s) is assumed to be constant at $0.78P_{atm}$. Using a zero-flux boundary condition at the bottom of the sediment and a constant CH₄ concentration equal to that in the overlying water layer at the sediment-water interface, the threshold depth $z_{eb,min}$ can then be solved numerically with a CH₄ concentration profile:

92
$$0=1-z_{eb,min}\alpha \exp(-z_{eb,min}\alpha)-\exp(-z_{eb,min}\alpha)-\alpha^2 \frac{k_{\text{diff,CH}_4}}{F_{Met,0}K_{\text{H,CH}_4}}P_{\text{res}}$$
 (S11)

where $P_{\text{res}} = \rho g h + P_{atm} - P_{\text{H2O}} - 0.78 P_{atm} - K_{H,\text{CH4}} [\text{CH}_4]$, and $k_{diff,\text{CH4}}$ is the effective molecular diffusion of CH₄. α is the shape parameter specifying the decay rate of CH₄ production rate versus sediment depth, and $F_{Met,0}$ is the maximum CH₄ production rate at the sediment-water interface. More details of the derivation of the above equations can be found in Langenegger *et al.* (2019).

S3. Two representative lakes: Deep oligotrophic lake in a cold climate vs. shallow eutrophic

lake in a warm climate

The model set-ups for these two representative lakes (a deep oligotrophic lake in a cold climate vs. a shallow eutrophic lake in a warm climate) are described in section 2.5.1, with their main results summarized in section 3.1. In this section, we introduce further details of numerical simulations related to these two representative lakes, i.e., the key physical–biogeochemical patterns as well as the seasonality of CH₄ productions and emissions.

S3.1 Physical-biogeochemical patterns of these two lakes

Here, we first illustrate the time series of mean water temperature (T_{mean}), mixing depth (z_{mix}), depth integrated primary production (F_{PP}) and mineralization (F_{Min}) as well as the labile carbon concentration ($C_{OC,auto}$) (Fig. 5 in the main text). For the deep oligotrophic lake, T_{mean} varies within a narrow range of ~3–8°C across seasons, while z_{mix} has a much larger variability comprised between 0.5m and 35m (i.e., h_{max}) (Fig. 5a in the main text). F_{PP} has a low yearly mean of ~13 gC m^{-2} yr⁻¹, with peaks during the productive season about twice as large. F_{Min} essentially follows the temporal evolution of F_{PP} , except with ~3 times lower peaks; however, the mineralization can also be higher than F_{PP} as high rates may persist for a longer duration (Fig. 5c in the main). As a result, the yearly mean of F_{min} amounts to 8 gC m⁻² yr⁻¹, with the difference between F_{PP} and F_{min} sustaining the burial flux and a weak accumulation in $C_{OC,auto}$ (Fig. 5e in the main). As a result of the dynamic interplay between F_{PP} and F_{Min} , the vertically homogeneous $C_{OC,auto}$ concentrations are comprised between 0.04 gC m⁻³ and 0.41 gC m⁻³, with a yearly mean of 0.19 gC m⁻³ (Fig. 5e in the main text).

For the shallow eutrophic lake, T_{mean} is characterized by much larger variations, ranging from 5° C in winter to ~15°C in summer, while in the mixed depth z_{mix} has a narrower range between 2 m in

warm seasons and 10 m in cold seasons (i.e., h_{max}) (Fig. 5b in the main). F_{PP} has a much higher yearly mean than the deep oligotrophic lake, reaching up to 490 gC m⁻² yr⁻¹, with peaks even exceeding 1000 gC m⁻² yr⁻¹ (Fig. 5d in the main text). F_{Min} also follows the temporal evolution of F_{PP} , with the yearly mean reaching 62% of F_{PP} . The dynamic balance between production and mineralization lead to $C_{OC,auto}$ concentration comprised between about 10 and 33 gC m⁻³ and a yearly mean of 21 gC m⁻³ (Fig. 5f in the main text).

Unsurprisingly, in the shallow eutrophic lake, T_{mean} responds more quickly to variations in T_a than in the deep lake because of a lower water volume. The dynamics of z_{mix} is more complex and requires investigating the vertical distribution of the temperature and density profiles (see below). In terms of biogeochemistry, the values of F_{PP} and $C_{OC,auto}$ simulated here are broadly consistent with those reported in the literature for lakes of similar characteristics (Wetzel, 2001). In shallow eutrophic lakes, the much higher F_{PP} and $C_{OC,auto}$ values are not only triggered by the higher phosphorus loads, but also by higher water temperatures, despite this latter factor also increasing F_{min} . Overall, the maximum $C_{OC,auto}$ concentrations in the eutrophic lake are about a factor of 100 larger than that in the oligotrophic lake, and these differences are instrumental in controlling the CH₄ production dynamics. The periods of significant $C_{OC,auto}$ densities (15 gC m⁻²) are also substantially longer in the eutrophic lake than in the oligotrophic lake.

In addition, FLaMe also reproduces observed vertical profiles of *T*, [O₂] and [CH₄] well (Fig. S9). In terms of physics and for both representative cases, as the temperature in the first water layer approaches 4°C, the thermocline (black curve in top panels) deepens sharply towards the lake bottom, effectively mixing the entire water column. In the deep oligotrophic lake (Fig. S9a, 9c, and 9e), stratification is almost permanently maintained and is only interrupted each year by short but intense

turnover events during late falls. In Winter, the stratification is particularly stable due to a long occurrence (six months) of ice cover; while in Summer, the stratification is gradually weakened as the warming of lake water occurs. The lake turnover events, by inducing full mixing across the entire water column, are key control factors of the spatio-temporal dynamics in O2 and CH4. Indeed, during lake turnovers, [O₂] is effectively mixed across all water layers and reach close to saturation concentrations with the atmosphere (14.6 and 9.1 g O₂ m⁻³ at a 0 and 20 °C, respectively). During the summer, slight oversaturation occurs in the upper portion of the lake as a result of photosynthetic activity, followed by a minimum in both the upper and deeper portions of the lake in the late summer/fall, when the mineralization rate (F_{Min}) is higher than the production rate (F_{PP}) and the oxygen diffusion from atmosphere cannot compensate oxygen net consumption. Except for this latter period, the combined effects of photosynthesis and transport from atmosphere via turnover events and eddy diffusion generally lead to well oxygenated conditions during most of the year, and the O₂ concentration is largely dominated by the solubility, itself controlled by the water temperature. That is, lake physics plays a dominant role in controlling the biogeochemical variables. Due to the oligotrophic status and well oxygenated conditions, the CH₄ concentrations are overall extremely low except near the lake bottom during the late summer/fall transition.

141

142

143

144

145

146

147

148

149

150

151

152

153

154

155

156

157

158

159

160

161

162

In the shallow eutrophic lake (Fig. S9b, 9d and 9f), there is no ice cover during the whole year due to a warmer climate, and the water temperature can adjust more quickly to the variations in atmospheric temperature due to lower lake depth. Thus, the stratification is weaker than in the deep oligotrophic lake, resulting in a less pronounced vertical gradients of water temperature. Similar to the deep oligotrophic lake, during summer and in the upper portion of the lake, the O₂ concentration are slightly supersaturated due to photosynthesis, followed by gradual decreases in O₂ concentration

as the F_{min} exceeds the F_{PP} . Due to the high production under eutrophic status, significant amounts of organic matter are exported to the lower portion of the lake (below thermocline), consuming progressively all of the O_2 and leading to the development of an anaerobic zone in the hypolimnion. That is, the vertical O_2 profile is controlled not only by the lake physics (temperature and O_2 solubility; as in the case of the deep oligotrophic lake) but also by the intense biogeochemical processes. As a result, the combined effects of high F_{Min} and low O_2 concentrations lead to maximal CH_4 concentrations (3.0 g CH_4 m⁻³) in late summer at the bottom of the lake, which are about 600-fold higher than that in the deep oligotrophic lake. In early Fall, the turnover events can bring oxygen down to lake bottom and abruptly interrupt the anaerobic condition for CH_4 production.

S3.2 Seasonality of CH₄ productions and emissions in these two lakes

The comparison of the seasonality in CH₄ productions and emissions for these two representative lakes is shown in Fig. S10. In the deep oligotrophic lake, the sedimentary CH₄ production ranges from 8.0×10⁻⁵ to 8.0×10⁻³ g CH₄ m⁻² d⁻¹, with the highest values in August and the lowest values in Winter and Spring. Due to the low production rate and high-water pressure, bubble formation is very limited and almost all the produced CH₄ escapes the sediment via diffusion. Since the oxygen availability is high throughout the year and the transport distance is long for the non-littoral zone of the lake, the diffusive CH₄ flux is almost completely oxidized before reaching the atmosphere. Moreover, the ice cover during winter and early spring (December–April) blocks the CH₄ emissions, such that all CH₄ emissions occur in the other seven months (May–November). As a result, the total CH₄ emissions range from 0 to 2.4×10⁻⁴ g CH₄ m⁻² d⁻¹ with a tiny peak in October, which results from lake turnovers and the additional contribution of the storage flux to diffusion.

In the shallow eutrophic lake, the CH₄ production is >1000 times higher than that in deep oligotrophic lake, ranging from 0.02 to 0.35 g CH₄ m⁻² d⁻¹. This much higher production is attributed to the higher nutrient loads, higher irradiance and higher temperature during summer which trigger higher F_{PP} , $C_{OC,auto}$, F_{Min} , and F_{Met} (Fig. 5 in the main text), and thus, higher F_{Met} under a lower O_2 concentration. This high CH₄ production not only favors CH₄ emissions crossing the sediment-water interface through the diffusive pathway $(F_{s,diff})$ but also through the ebullitive pathway $(F_{s,ebul})$. Compared to the deep oligotrophic lake, the shallow eutrophic lake also has weaker stratification, shorter transport distance from sediment to atmosphere (in non-littoral zones), and therefore a lower fraction of diffusive CH₄ is oxidized, leading to ~900 times higher total CH₄ emissions. Moreover, the total emissions have a seasonal pattern similar to that of production, with highest (0.21 g CH₄ m⁻¹ ² d⁻¹) and lowest (0.02 g CH₄ m⁻² d⁻¹) emissions in September and February, respectively. Due to the warm climate, the water temperature is too high to form ice on the lake surface, leading to emissions during the whole year, about twice longer than for the deep oligotrophic lake under cold climate. Overall, with these two representative lakes, we show that FLaMe can well capture the wide range of CH₄ emissions (0–0.3 g CH₄ m⁻² d⁻¹) from oligotrophic to eutrophic lakes in real world, as demonstrated by the cases in Tan et al. (2024).

185

186

187

188

189

190

191

192

193

194

195

196

197

198

199

200

S4. Effects of trophic status, lake depths, climate conditions on seasonal CH₄ dynamics

In this section, we illustrate the responses of CH₄ dynamics to variations in environmental gradients and lake morphology, hence decomposing the collective effects of these environmental factors analyzed in section S3). First, we set as baseline case a mesotrophic lake with $h_{max} = 15$ m (and $h_{mean} = 7.5$ m), [TP]=30 µgP L⁻¹, forced by a temperate climate (48.75°N, 8.75°E) (Fig. S3). Based on this baseline, we then explore the responses of the CH₄ dynamics induced by individual effects of trophic status, climate condition and lake depth, by varying one parameter at a time: (1) increasing the [TP] from 8 to 80 µg P L⁻¹; and (2) changing the climate from warm (43.75°N, -6.25°E; Fig. S1) to cold conditions (63.75°N, 26.25°E; Fig. S2); (3) changing the maximal lake depth (h_{max}) from 10 to 35 m;.

S4.1 Baseline of lake CH₄ seasonality

In this baseline (Fig. S11), the CH₄ production in lake sediment has its highest rates (0.08 g CH₄ m⁻² d⁻¹) in September and lowest rates (0.003 g CH₄ m⁻² d⁻¹) in March. The seasonal patterns of CH₄ emissions follows those of CH₄ production, but they are interrupted by the storage flux induced by the weakened stratification and turnover during late fall. As a result, the CH₄ emissions are highest (0.04 g CH₄ m⁻² d⁻¹) in November and lowest (0.001 g CH₄ m⁻² d⁻¹) in March. Overall, annual mean CH₄ production and emission are 0.037 g CH₄ m⁻² d⁻¹, and 0.019 g CH₄ m⁻² d⁻¹, respectively, with the peaks of total CH₄ production and emission about 3 and 2 times higher than their means. The magnitudes of CH₄ emissions in this mesotrophic lake are very close to the cases (Erssjön and Fei-Tsui) as demonstrated by Tan *et al.* (2024).

S4.2 Effects of trophic status on CH₄ seasonality

Under different trophic status, the total CH₄ productions have similar seasonality (Fig. S12) as

that of the baseline case (Fig. S11), with peaks and valleys of CH₄ production in August and February, respectively. From oligotrophic to trophic status ([TDP] is increased by 10 times), the peak of CH₄ production grows by a factor of 18 (from 0.013 to 0.24 g CH₄ m⁻² d⁻¹), and the mean of CH₄ production is increased by a factor of 30 (from 0.003 to 0.089 g CH₄ m⁻² d⁻¹). This nonlinear response of CH₄ production to [TDP] can be explained by the effect of P limitation on F_{PP} (see Eq. (3) in the main) (6 times, from 0.08 to 0.47 from oligotrophic to eutrophic status), as well as the oxygen control on benthic CH₄ production, i.e., the bottom oxygen concentration is much lower and the anoxic condition persists for a longer time in the eutrophic lake (Fig. S16a vs. 16b). In the oligotrophic lake, the peak of CH₄ emission occurs in September, indicating a one-month time lag compared to the production, which is attributed to the lake stratification and inhibited transport from lake bottom to surface. The blocking effect of lake stratification on CH₄ emissions is more evident when the CH₄ production is higher in the eutrophic lake, postponing the peak of CH₄ emissions to November.

As shown in Fig. S12, the ratio of ebullition to diffusion from sediments is also sensitive to the trophic status, suggesting a higher (78%) fraction of diffusion for the oligotrophic case compared to the eutrophic case (59%). This is expected because, due to higher production and lower oxygen compared to the oligotrophic case, the CH₄ production is much higher in the eutrophic case, thus promoting much higher CH₄ supersaturation and bubble production (indicated by lower $z_{\text{cb,min}}$). The oligotrophic and eutrophic lakes have similar seasonal patterns of CH₄ emissions except the high storage flux occurred in eutrophic case. The oligotrophic lake has slightly higher shares (60% vs. 56%) of ebullition to atmosphere highlighting the more efficient CH₄ oxidation in the water column for the oligotrophic lake, as revealed in Fig. S16.

S4.3 Effects of climate conditions on CH₄ seasonality

The climate condition changes not only the magnitudes of CH₄ production and emission but also the temporal patterns or seasonality (Fig. S13). From cold to warm climate, the peak of CH₄ production grows by a factor of 4 (0.04 to 0.17 g CH₄ m⁻² d⁻¹), and the mean of CH₄ production grows by a factor of 6 (0.0094 to 0.059 g CH₄ m⁻² d⁻¹), which is mainly attributed to the higher solar radiation and temperature (Fig. S1 and Fig. S2). Across this climate gradient, both the peak and mean of CH₄ emissions grow by a factor of ~4 (from 0.02 to 0.07 g CH₄ m⁻² d⁻¹ and from 0.0057 to 0.03 g CH₄ m⁻² d⁻¹). This implies that a larger fraction of CH₄ production is oxidized in the warmer lake, due to higher water temperature (Fig. S15). Climate also controls the ratio of ebullition to diffusion in production, with the ebullitive pathway being favored by higher temperature in warmer climate (42% versus 36%) (through lower gas solubility and higher methanogenesis). After accounting for CH₄ oxidations during diffusion, the fraction of ebullition in CH₄ emissions is still higher in warmer climate (78% vs. 65%), probably due to the higher CH₄ oxidation rate during the diffusive transport in water column in the warmer lake.

Driven by a cold climate in the boreal region (Fig. S13a), the seasonality of CH₄ production and emissions are highly affected by the ice cover in winter and spring when the methanogenesis is strongly reduced due to low temperature and emissions are blocked by the ice. The CH₄ production starts to increase from June, reaches its maximum in August, and returns to a low level in December. The CH₄ emissions follow the seasonal pattern of production but is interrupted by the storage flux induced by lake stratification, leading to a peak in October. With a warmer climate (located in the temperate region) (Fig. S13b), both CH₄ productions and emissions have later peaks (September and November, respectively). In the warmer lake, the contribution of the storage flux is more evident,

probably due to higher CH₄ production during summer coinciding with the period of strong lake stratification.

S4.4 Effects of lake depth on CH₄ seasonality

By comparing Fig. S14b and Fig. S11, we found that the lakes with a maximum depth of 15 m and 35 m have almost the same CH₄ production rate (0.03 g CH₄ m⁻² d⁻¹ for the mean and 0.08 g CH₄ m⁻² d⁻¹ for the peak), consistent with our common knowledge and the inferences from formulas of depth-integrated F_{PP} , F_{Min} , and F_{Met} (Eqs. (3), (8), and (9) in the main). However, the lake with a shallower depth ($h_{max} = 10$ m) has a slightly lower CH₄ production rate (0.025 g CH₄ m⁻² d⁻¹ for the mean and 0.07 g CH₄ m⁻² d⁻¹ for the peak). This is attributed to the photic zone being truncated by morphological constraints (i.e., the lakebed is shallower than the "natural" photic depth), which decreases the depth-integrated primary production and further the mineralization and CH₄ production (note that our model does not account for benthic algal production). Lake depth has a more evident effect on the fraction of sedimentary CH₄ production channeled into the ebullitive pathway (52% versus 28%), because this pathway is favored in a shallower lake with lower CH₄ solubility due to higher temperature and lower hydrostatic pressure.

Consistent with our common knowledge, the CH₄ emissions are overall lower for a deeper lake, due to the higher CH₄ solubility, efficient oxidation during the diffusive transport of CH₄ through longer distance, and larger dissolution of the ebullitive flux during the transport of gas bubbles. Interestingly, the lower CH₄ emissions in the deeper lake during the production season could be attributed to a stronger lake stratification, and this effect may also be reflected by the more evident storage flux in November, December and January, which partly offsets the lower emissions of the deeper lake in other months of the year. Except for these three months, the fraction of ebullitive

emissions is slightly higher in deeper lakes (87% vs. 84%), despite a lower fraction of ebullition in the production. However, if we take these three months into account, the fraction of ebullitive emissions in deeper lake becomes 64%, much lower than that in shallower lake (82%). This implies that the lake stratification also plays a crucial role in the regulating the emission pathways especially for deep lakes.

S5. Estimates of CH₄ emissions from large lakes (≥1000 km²) within European domain

- To estimate CH₄ emissions from European lakes ≥1000 km², we came up with two strategies as follows:
- (1) We used FLaMe model directly to simulate lakes $\geq 1000 \text{ km}^2$ within the European domain and found that the CH₄ emissions from European lakes $\geq 1000 \text{ km}^2$ accounts for only 6% of those from smaller lakes, i.e., 0.06 Tg CH₄ yr⁻¹. Thus, the European lakes have a total CH₄ emissions of 1.03 Tg CH₄ yr⁻¹.
- (2) Despite with very limited samples, Johnson *et al.* (2022) found that the total CH₄ emission (sum of diffusion and ebullition) rates per unit area from lakes $\geq 5000 \text{ km}^2$ are in the range of 0–25% of emissions from smaller lakes. Following Johnson *et al.* (2022), we assumed that the CH₄ emission rates per unit area from lakes $\geq 1000 \text{ km}^2$ falls in the higher end of 0–25% and adopt a value of 20% to estimate the CH₄ emission rates for lakes $\geq 1000 \text{ km}^2$.
- From our simulations for lakes smaller than $<1000 \text{ km}^2$, we obtained that the mean CH₄ emission rate per unit lake area amounts to 7.39 g CH₄ m⁻² yr⁻¹. Thus, the mean CH₄ emission rate per unit lake area for lakes larger than 1000 km^2 is estimated as $7.39 \cdot 20\% = 1.48 \text{ g CH}_4 \text{ m}^{-2} \text{ yr}^{-1}$. By multiplying this mean CH₄ emission rate (1.48 g CH₄ m⁻² yr⁻¹) with the area of $0.88 \cdot 10^5 \text{ km}^2$ for lakes $\ge 1000 \text{ km}^2$,

we obtain CH₄ emissions from large lakes as 0.13 Tg CH₄ yr⁻¹, broadly similar to what is obtained with the first method. Thus, the European lake emissions reach in this case a total CH₄ of 1.10 Tg CH₄ yr⁻¹.

312

313

314

Combining these two strategies, we provide a back of the envelope estimate for the total CH₄ emissions from European lakes as 1.03–1.10 Tg CH₄ yr⁻¹, which can be directly compared to previous estimates.

315 References

- Langenegger, T., Vachon, D., Donis, D., and McGinnis, D. F.: What the bubble knows: Lake methane dynamics
- 317 revealed by sediment gas bubble composition. Limnol. Oceanogr., 64: 1526-
- 318 1544. https://doi.org/10.1002/lno.11133,_2019.
- MacKay, M. D., Verseghy, D. L., Fortin, V., and Rennie, M. D.: Wintertime simulations of a boreal lake with
- the Canadian Small Lake Model, J. Hydrometeorol., 18, 2143–2160, https://doi.org/10.1175/JHM-D-16-
- 321 0268.1, 2017.
- MacKay, M. D.: A process-oriented small lake scheme for coupled climate modeling applications, J.
- 323 *Hydrometeorol.*, 13, 1911–1924, https://doi.org/10.1175/JHM-D-11-0116.1, 2012.
- Tan, Z., Yao, H., Melack, J., Grossart, H.-P., Jansen, J., Balathandayuthabani, S., Sargsyan, K., and Leung, L.
- R.: A lake biogeochemistry model for global methane emissions: Model development, site-level
- validation, and global applicability. J. Adv. Model. Earth Syst., 16, e2024MS004275. https://doi.org/
- 327 10.1029/2024MS004275, 2024.
- Wetzel, R.G.: Limnology: Lake and river ecosystems (Third Edition), Academic Press, San Diego, p389,
- 329 https://doi.org/10.1016/C2009-0-02112-6, 2001.

Fig. S1. Meteorological data (2012-2016) for a cold climate (63.75°N, 26.25°E) extracted from the ISIMIP3a. (a) long-wave radiation ($F_{\lambda,long}$); (b) short-wave radiation ($F_{\lambda,short}$) (c) atmospheric temperature near the surface (T_a); (d) precipitation (P_r); (e) specific humidity (h_s); and (f) near-surface wind (U_a).

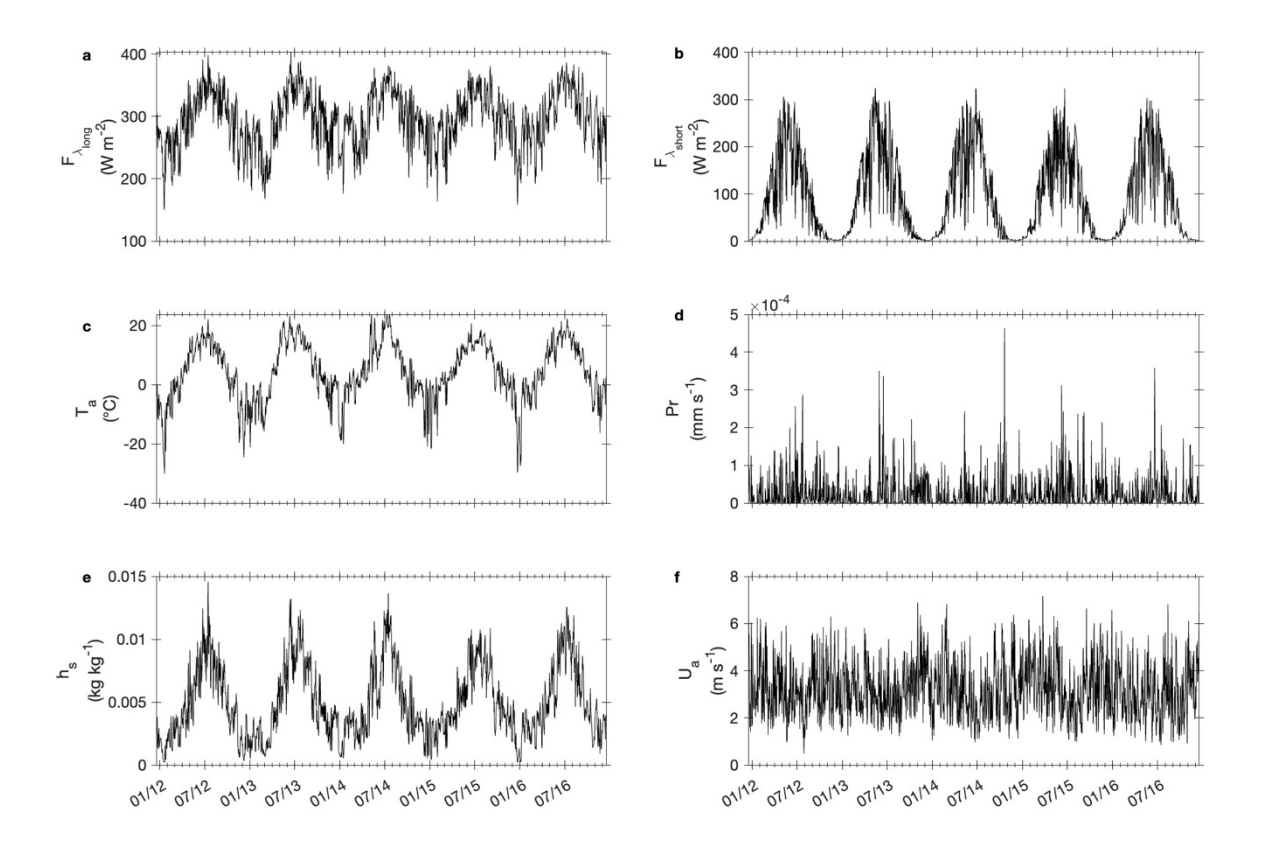


Fig. S2. Meteorological data (2012-2016) for a warm temperate climate (43.75°N, -6.25°E) extracted from the ISIMIP3a. (a) long-wave radiation ($F_{\lambda,long}$); (b) short-wave radiation ($F_{\lambda,short}$) (c) atmospheric temperature near the surface (T_a); (d) precipitation (P_r); (e) specific humidity (h_s); and (f) near-surface wind (U_a).

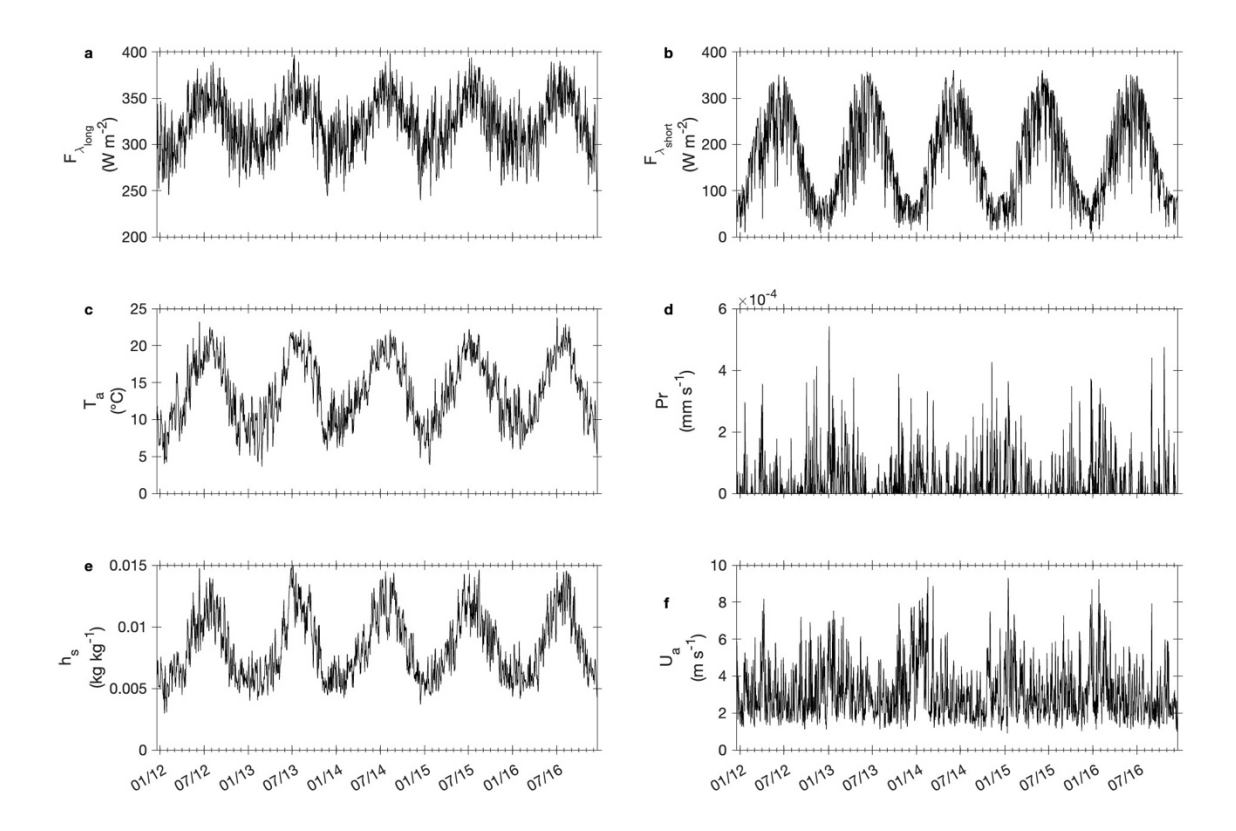


Fig. S3. Meteorological data (2012-2016) in Finland (48.75°N, 8.75°E) extracted from the ISIMIP3a. (a) long-wave radiation ($F_{\lambda,long}$); (b) short-wave radiation ($F_{\lambda,short}$) (c) atmospheric temperature near the surface (T_a); (d) precipitation (P_r); (e) specific humidity (h_s); and (f) near-surface wind (U_a).

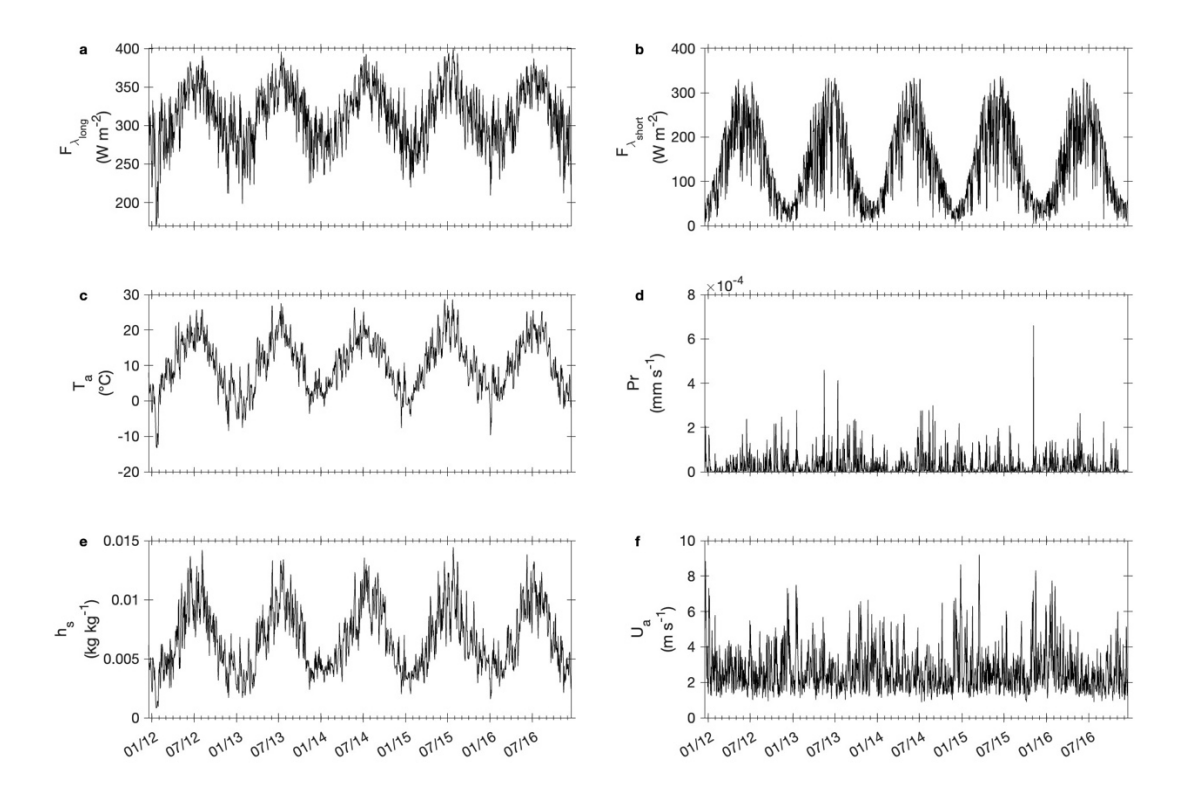


Fig. S4. Spatial distribution of lake areas within the European domain. (a) Lake area within each grid cell (km⁻²); (b) Land area within each grid cell (km⁻²); (c) The ratio of lake area to land area within each grid cell.

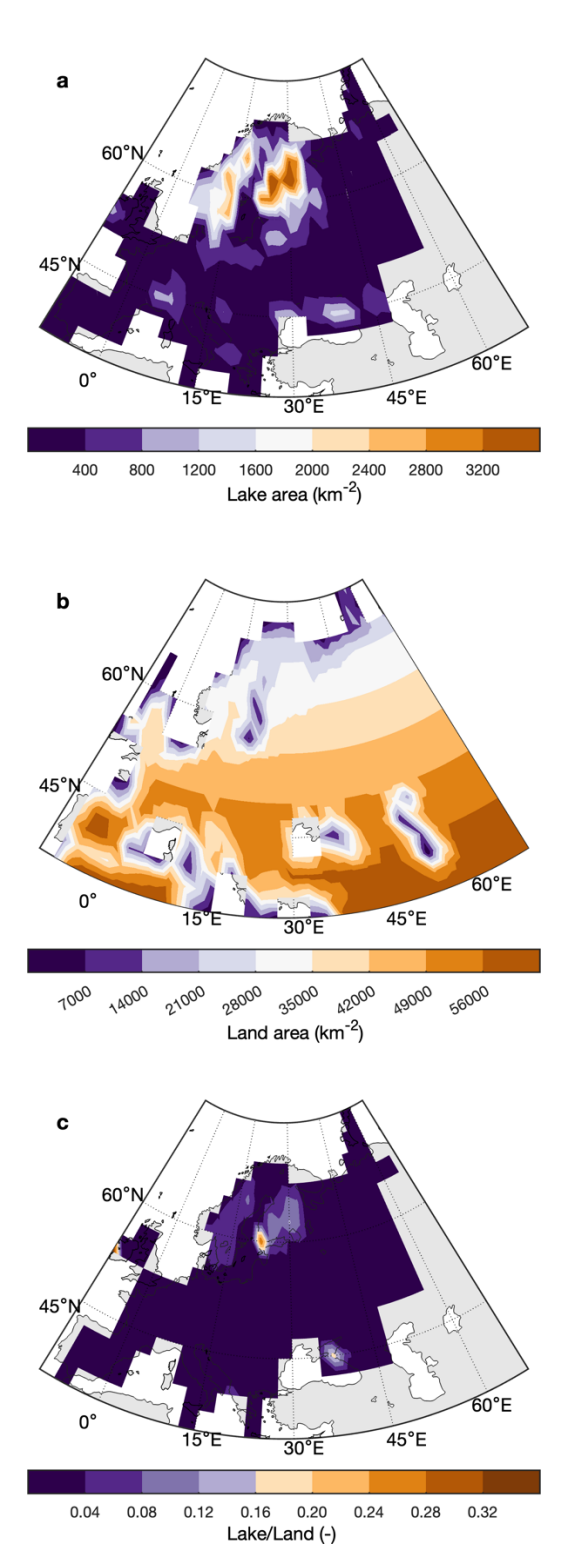


Fig. S5. Frequency distributions of lake area and depth within European domain. Frequency distributions of (a) lake area (km²), (b) depth (m), (c) lake area ($log_{10}(km^2)$), and (d) lake depth ($log_{10}(m)$).

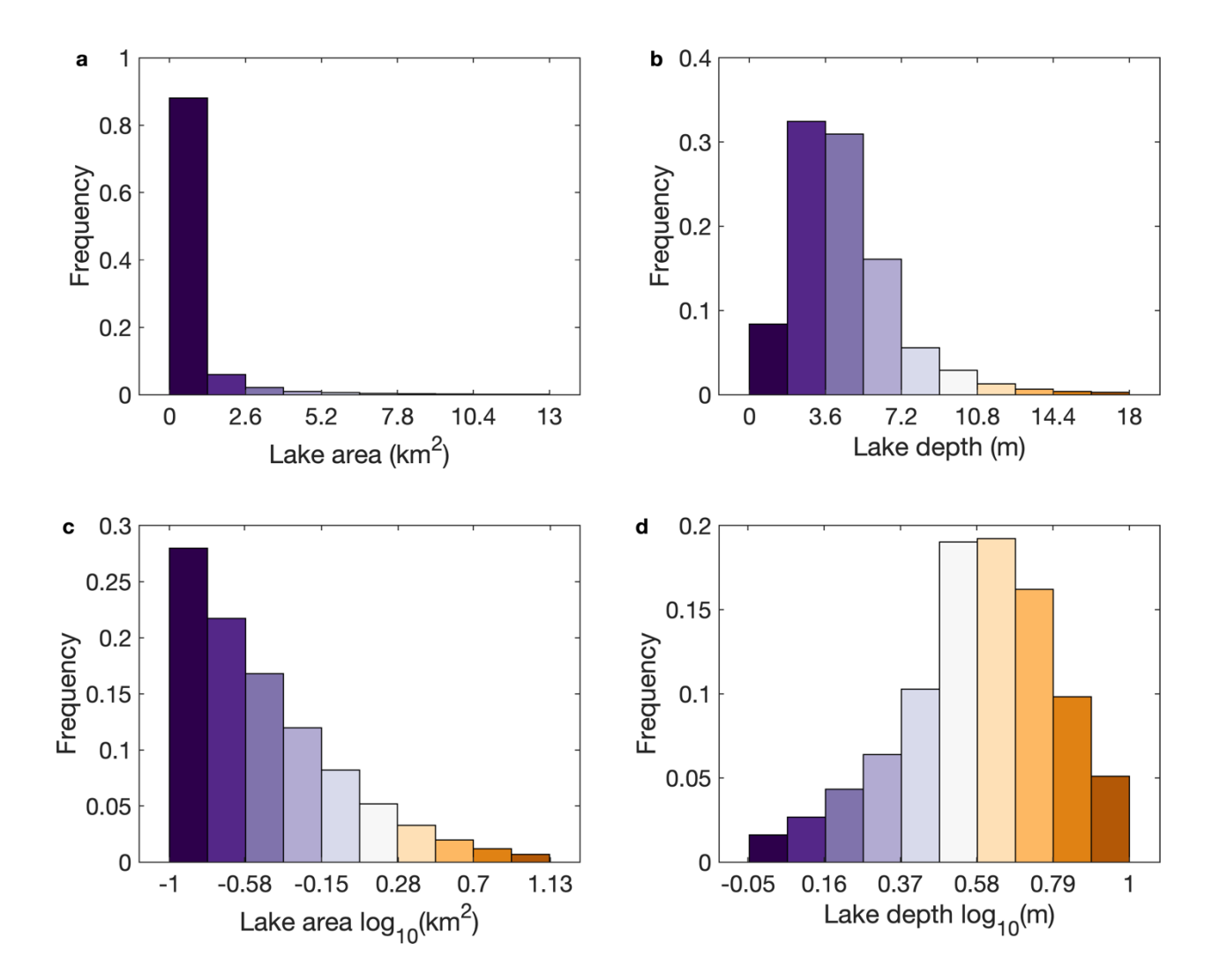


Fig. S6. Spatial distribution of climate forcings in the European domain. (a) Short wave radiation (W m⁻²); (b) Long wave radiation (W m⁻²); (c) Air temperature (°C); (d) Precipitation (mm yr⁻¹); (e) Wind speed (m s⁻¹); (f) Specific humidity (kg kg⁻¹).

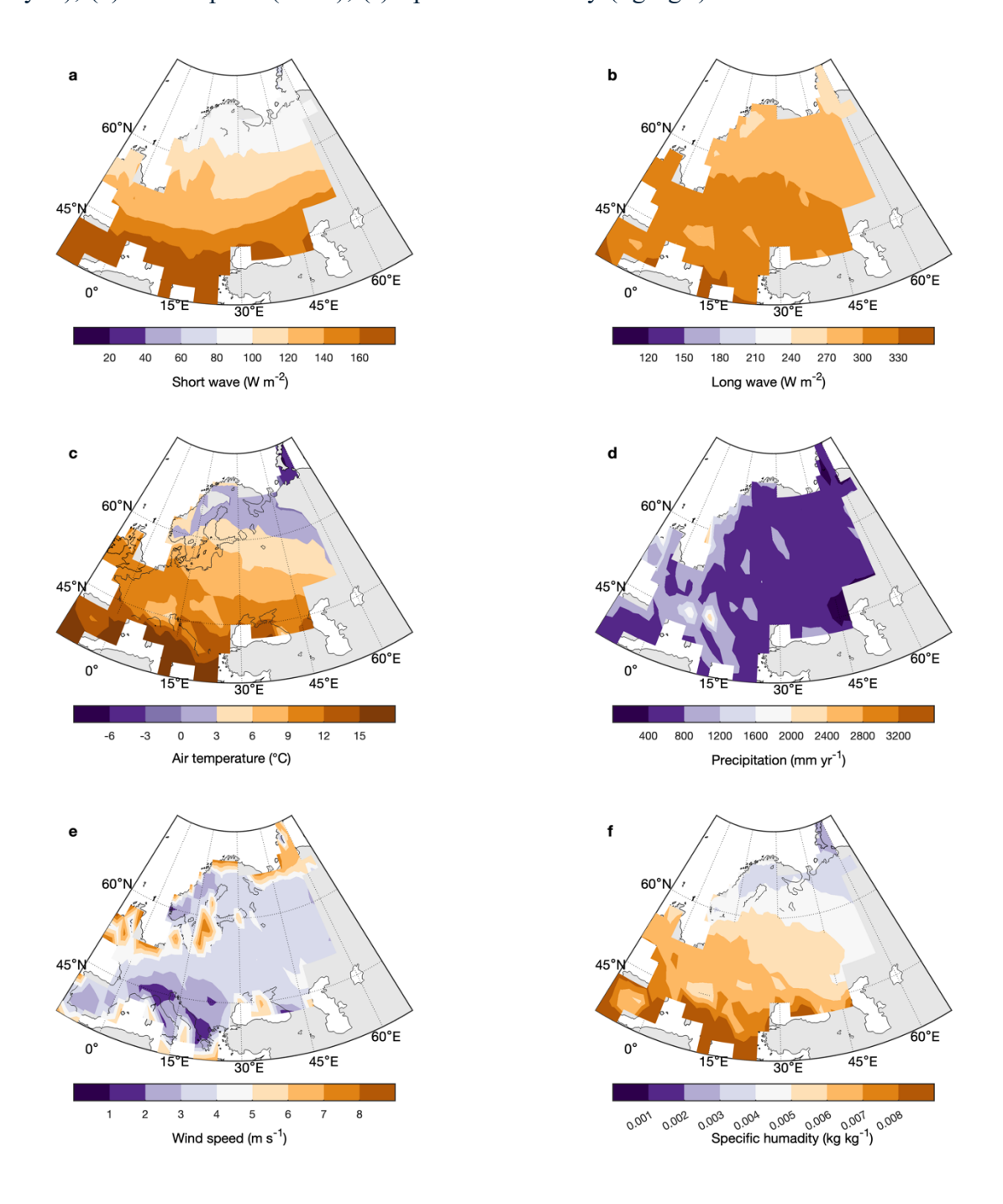
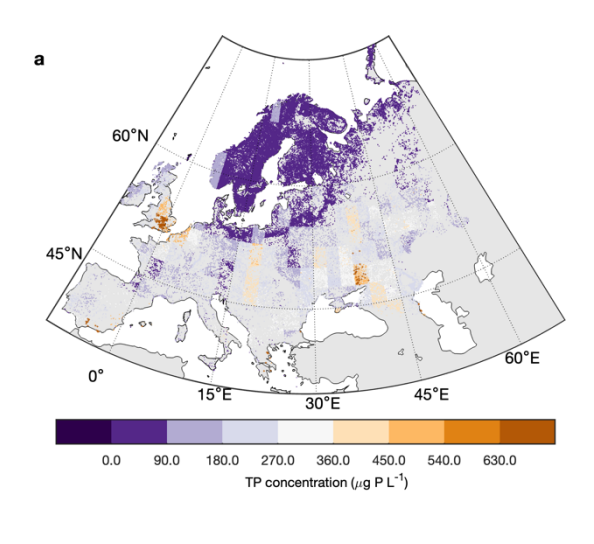


Fig. S7. Spatial distribution of (a) total phosphorus concentration ([TP], μg L⁻¹) and (b) P limitation in European lakes. The P limitation is evaluated based on the Michaelis-Menten equation with total phosphorus concentration from IMAGE-GNM model.



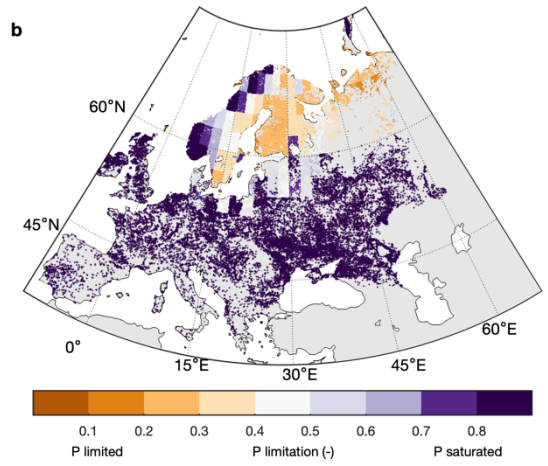


Fig. S8. Frequency distribution of total phosphorus concentration (TP; g P m⁻³) for lakes of different sizes. (a) Class 1: 0.1–1 km²; (b) Class 2: 1–10 km²; (c) Class 3: 10–100 km²; (d) Class 4: 100–1000 km².

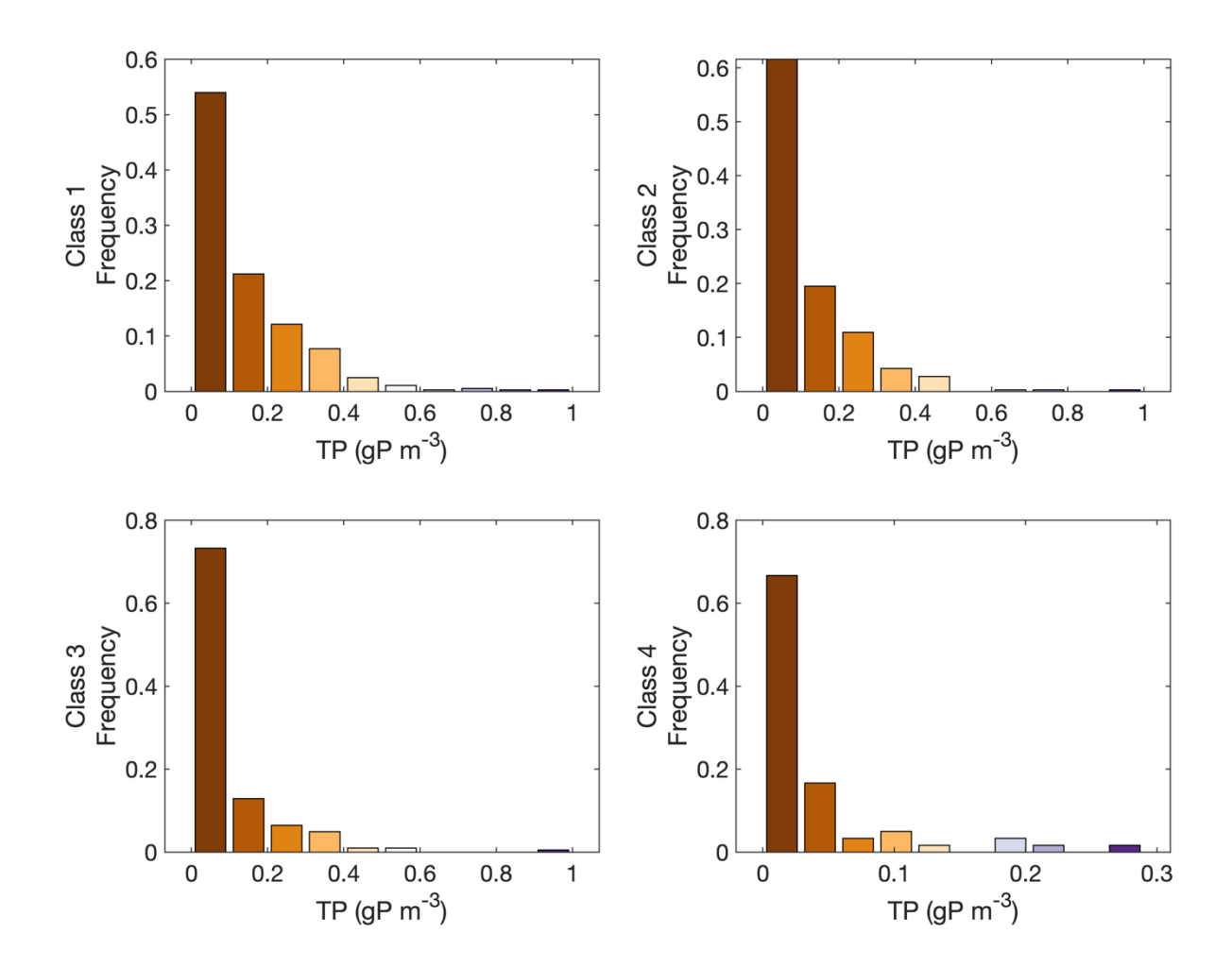


Fig. S9. Vertical profiles of T, $[O_2]$ and $[CH_4]$ for the deep oligotrophic lake (left) and the shallow eutrophic lake (right). Top row: Temperature, mixing depth (black line), photic depth (red curve) and period of ice cover (grey shaded areas at the lake surface). Middle row: Oxygen. Bottom row: CH_4 . *Note the different scales for CH_4 in panels e and f.*

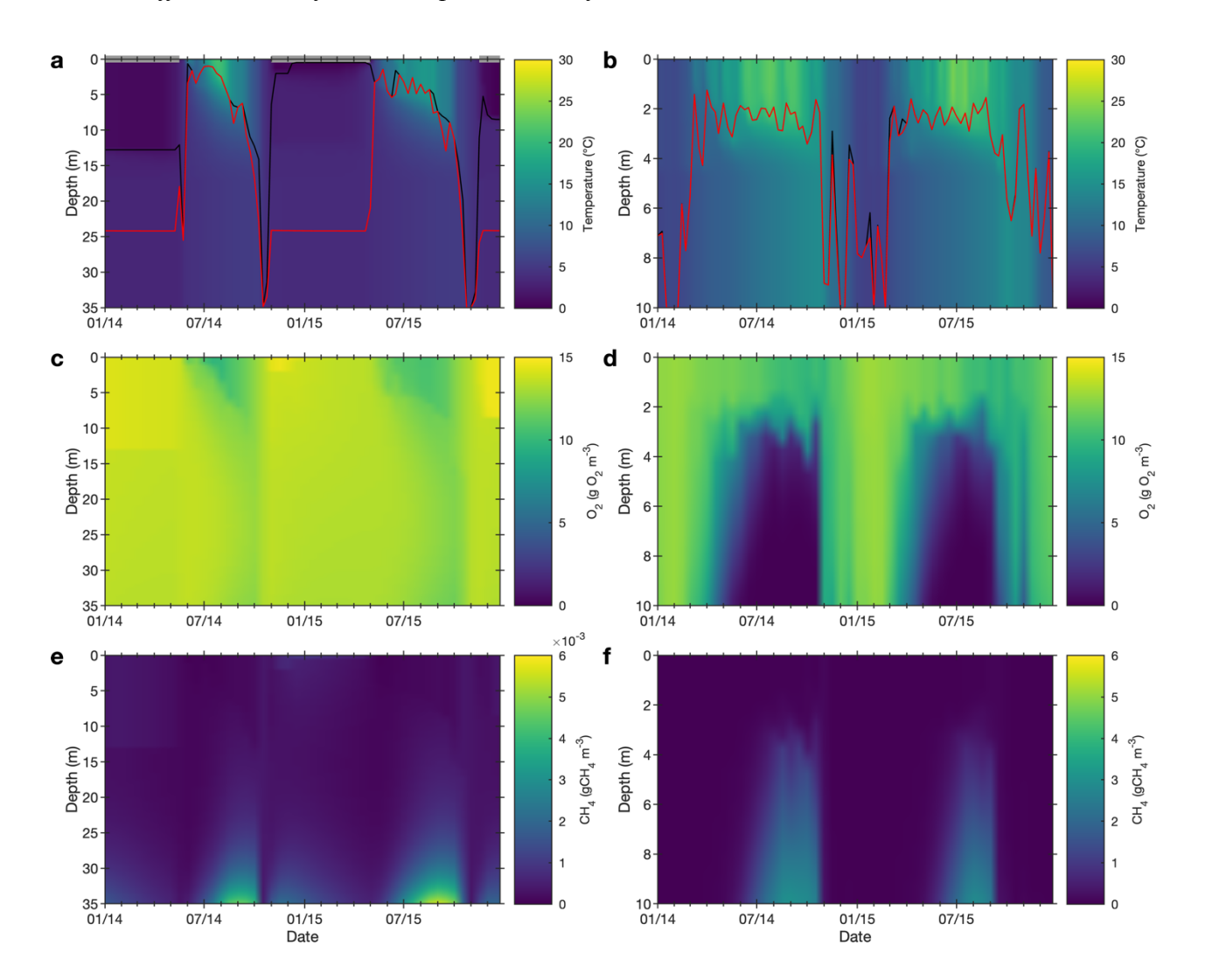


Fig. S10. Comparison of seasonality of sedimentary methane (CH₄) production (fainted colors) and CH₄ emissions to the atmosphere (plain colors) for the two representative lakes. (a) deep oligotrophic lake, driven by a cold climate (63.75°N, 26.25°E), and (b) the shallow eutrophic lake, driven by a warm climate (43.75°N, -6.25°E). Orange: diffusive flux; Cyan: Ebullitive flux. Dashed curve: Percent days with ice cover. *Note the different scales in panels a and b*.

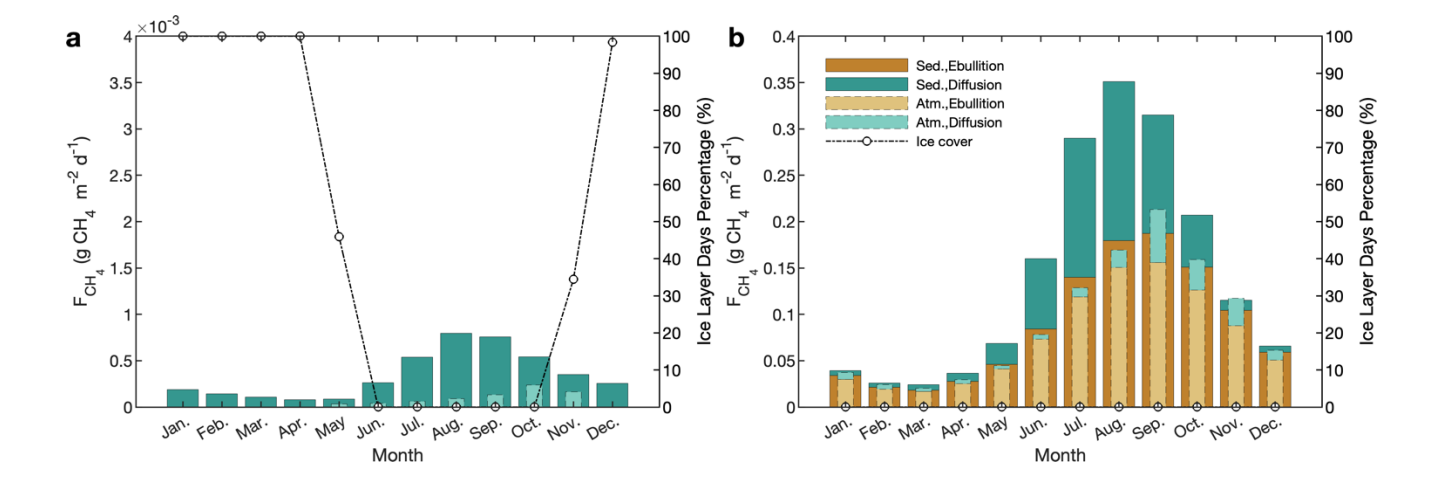


Fig. S11. Baseline of the seasonality of CH₄ productions and emissions. The baseline mesotrophic lake has a maximal depth of 15 m (a mean depth of 7.5 m), and a [TDP] of 30 μ g P L⁻¹, and climate forcings at the grid cell of 48.75°N, 8.75°E. Note that the diffusive emission is higher than the production in November, indicating the occurrence of storage flux due to lake turnover.

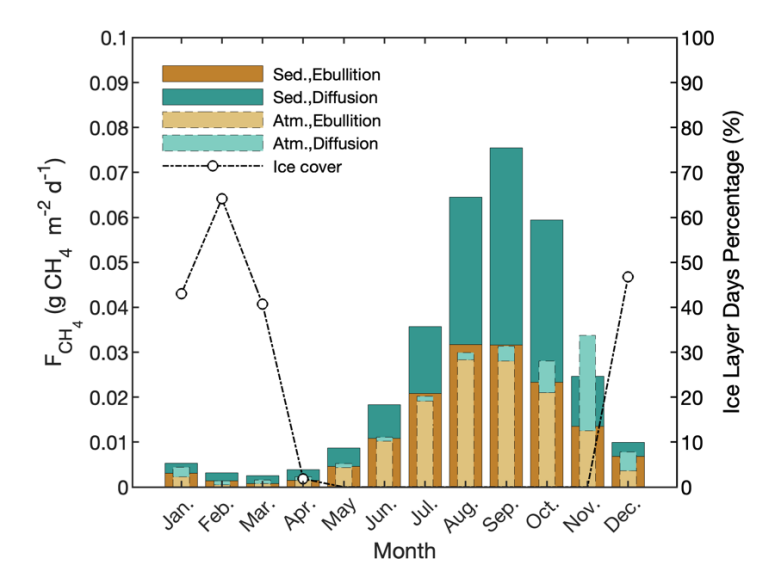


Fig. S12. Effects of lake trophic status on CH₄ dynamics. The lake has a [TDP] of (a) $8 \mu gP L^{-1}$ and (b) $80 \mu gP L^{-1}$. The lake depth, area and climate conditions are set the same as those in the baseline. Note that the diffusive emission is higher than the production in November and December, indicating the occurrence of storage flux due to lake turnover. *Note the different scales in panels a and b*.

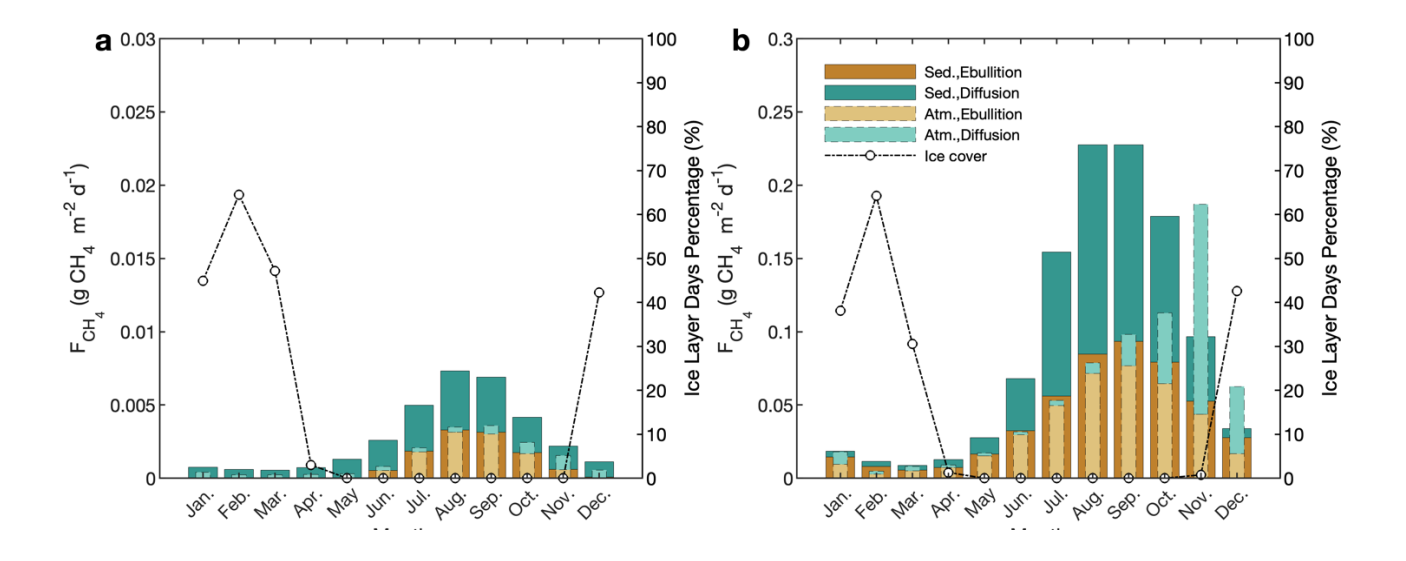


Fig. S13. Effects of climate conditions on CH₄ dynamics. The climate conditions are set as (a) warm $(43.75^{\circ}N, -6.25^{\circ}E)$ and (b) cold $(63.75^{\circ}N, 26.25^{\circ}E)$. The [TDP] and lake depth are set the same as those in the baseline. Note that the higher diffusive emission than the production (October in a and November in b) indicates the occurrence of storage flux due to lake turnover.

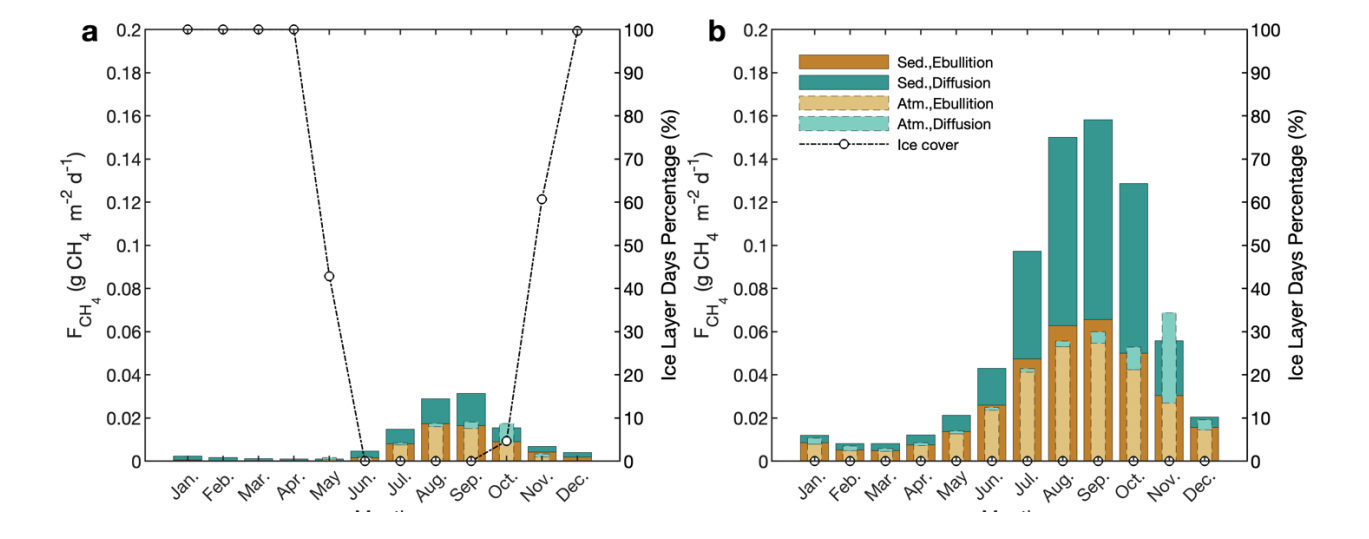


Fig. S14. Effects of lake depth on CH₄ dynamics. The lake depth is set as (a) $h_{\text{max}} = 10 \text{ m}$ ($h_{\text{mean}} = 5 \text{ m}$) and (b) $h_{\text{max}} = 35 \text{ m}$ ($h_{\text{mean}} = 17.5 \text{ m}$). The [TDP] and climate conditions are set the same as those in the baseline. Note that the higher diffusive emission than the production indicates the occurrence of storage flux due to lake turnover.

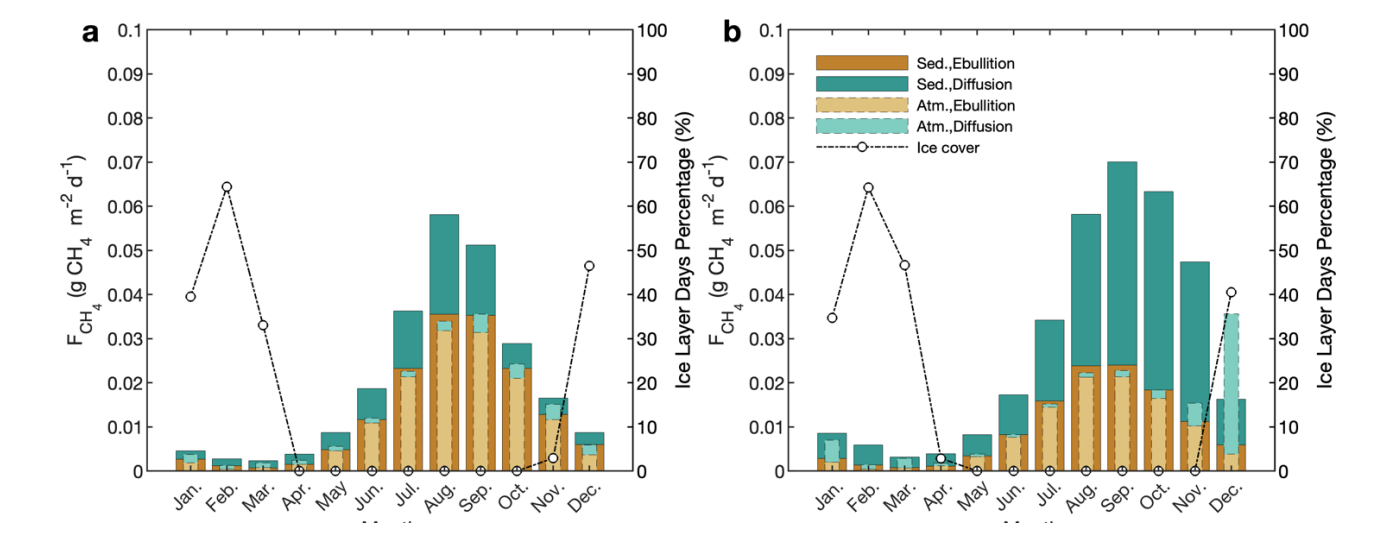


Fig. S15. Vertical profiles of lake temperature across environmental gradients. (a) and (b): Lakes with different trophic status ([TDP]=8 μ g L⁻¹ and 80 μ g L⁻¹); (c) and (d): Lakes driven by different climate condition (cold vs. warm climate); (e) and (f): Lakes with different depth (10 m vs. 35 m).

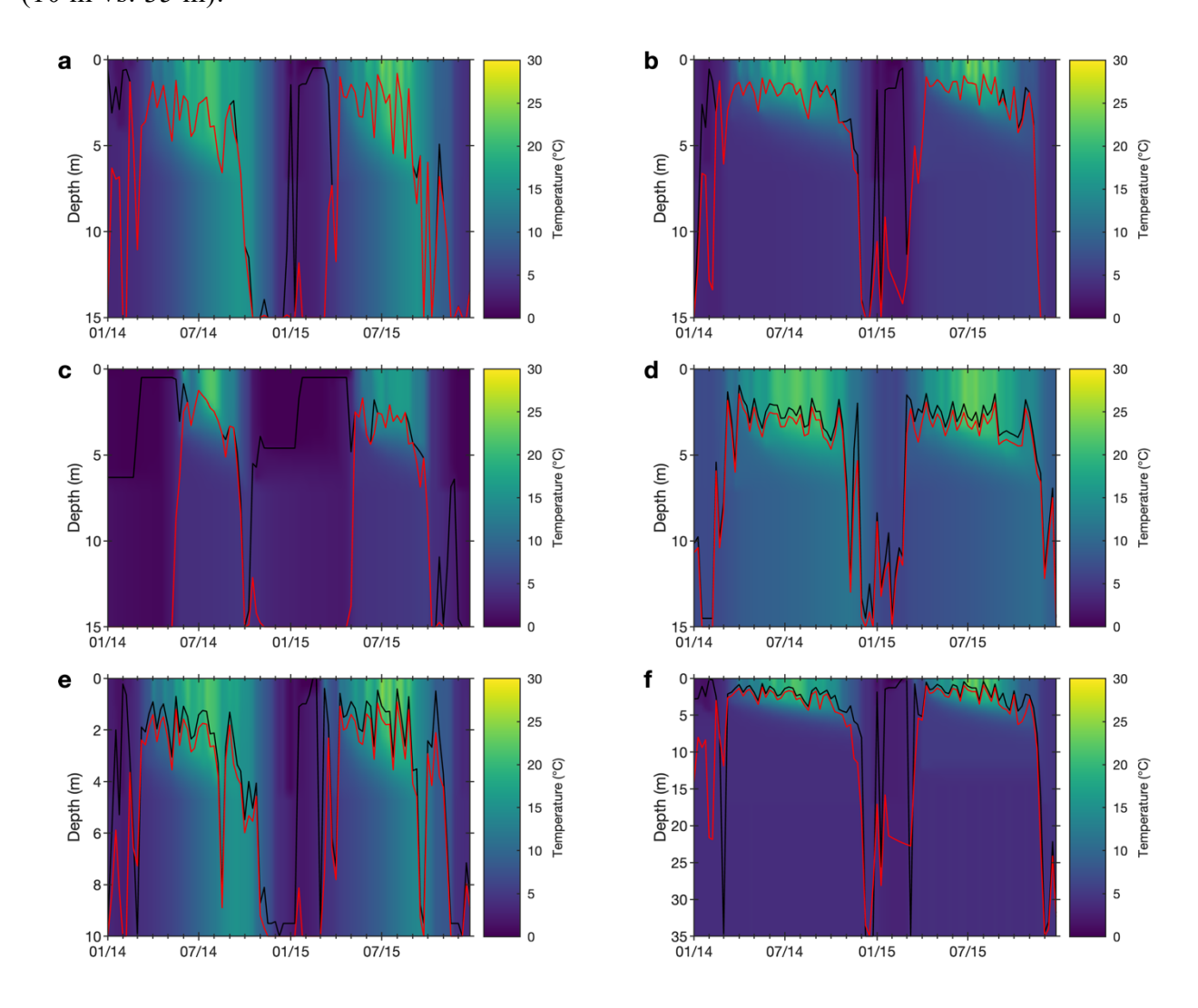


Fig. S16. Vertical lake oxygen profiles across environmental gradients. (a) and (b): Lakes with different trophic status ([TDP]=8 μ g L⁻¹ and 80 μ g L⁻¹); (c) and (d): Lakes driven by different climate condition (cold vs. warm climate); (e) and (f): Lakes with different depth (10 m vs. 35 m).

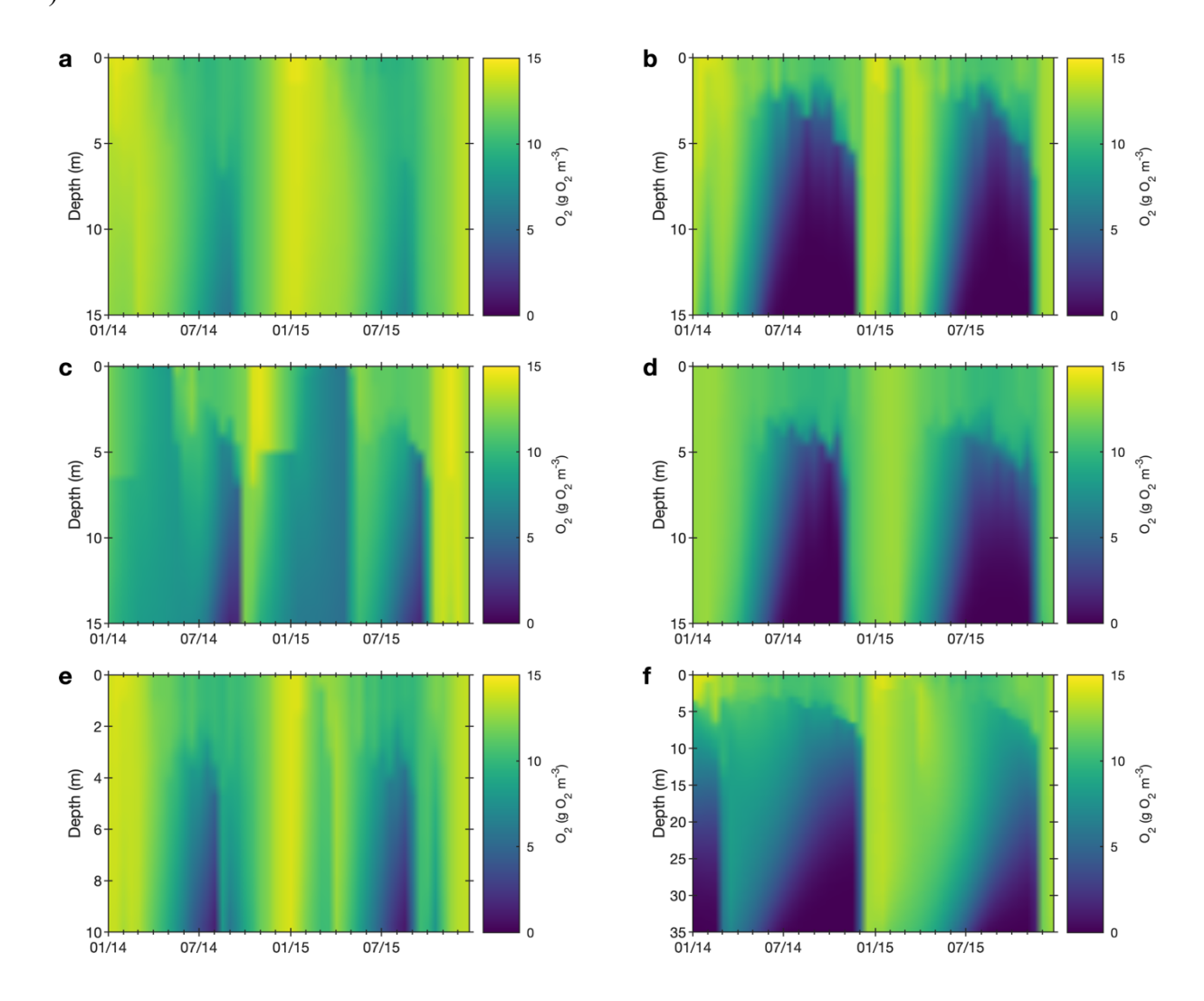


Fig. S17. Vertical lake methane profiles across environmental gradients. (a) and (b): Lakes with different trophic status ([TDP]=8 μ g L⁻¹ and 80 μ g L⁻¹); (c) and (d): Lakes driven by different climate condition (cold vs. warm climate); (e) and (f): Lakes with different depth (10 m vs. 35 m).

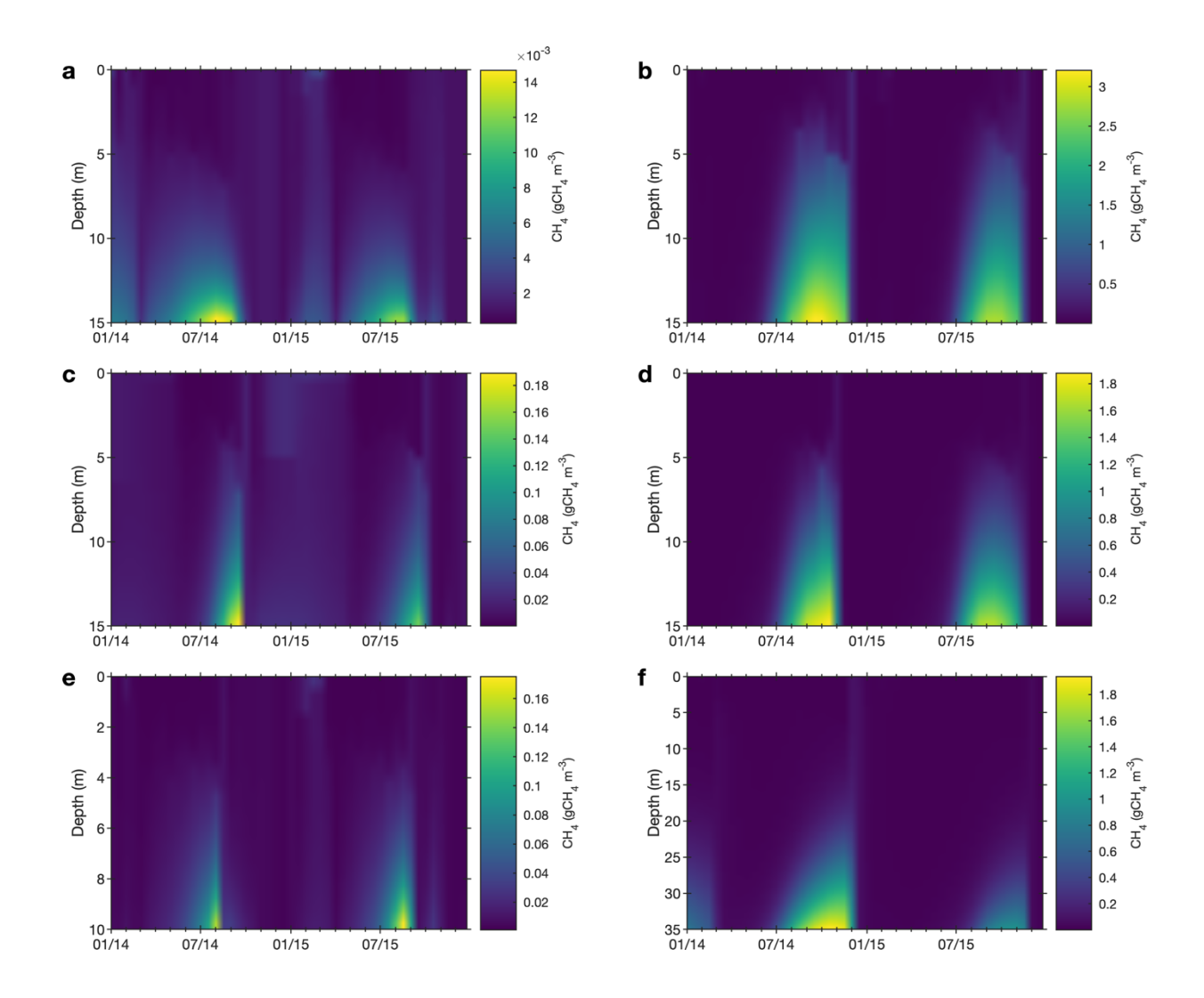


Fig. S18. Comparison of simulated depth-integrated primary production (F_{PP}) with empirical estimates reported by Wetzel (2001). The histograms show the frequency distributions of simulated F_{PP} (log scale) in all European lakes (n = 108407) that are grouped into ultraoligotrophic (0–5 µgP L⁻¹), oligotrophic (5–10 µgP L⁻¹), mesotrophic (10–30 µgP L⁻¹), and eutrophic (>30 µgP L⁻¹) lakes. In the figure, blue and red dashed lines are the lower and upper bounds (LB_{obs} and UB_{obs}), respectively; Black solid and dotted lines are the median_{mod} and mean_{mod}, respectively, of simulated F_{PP} in this class of lakes.

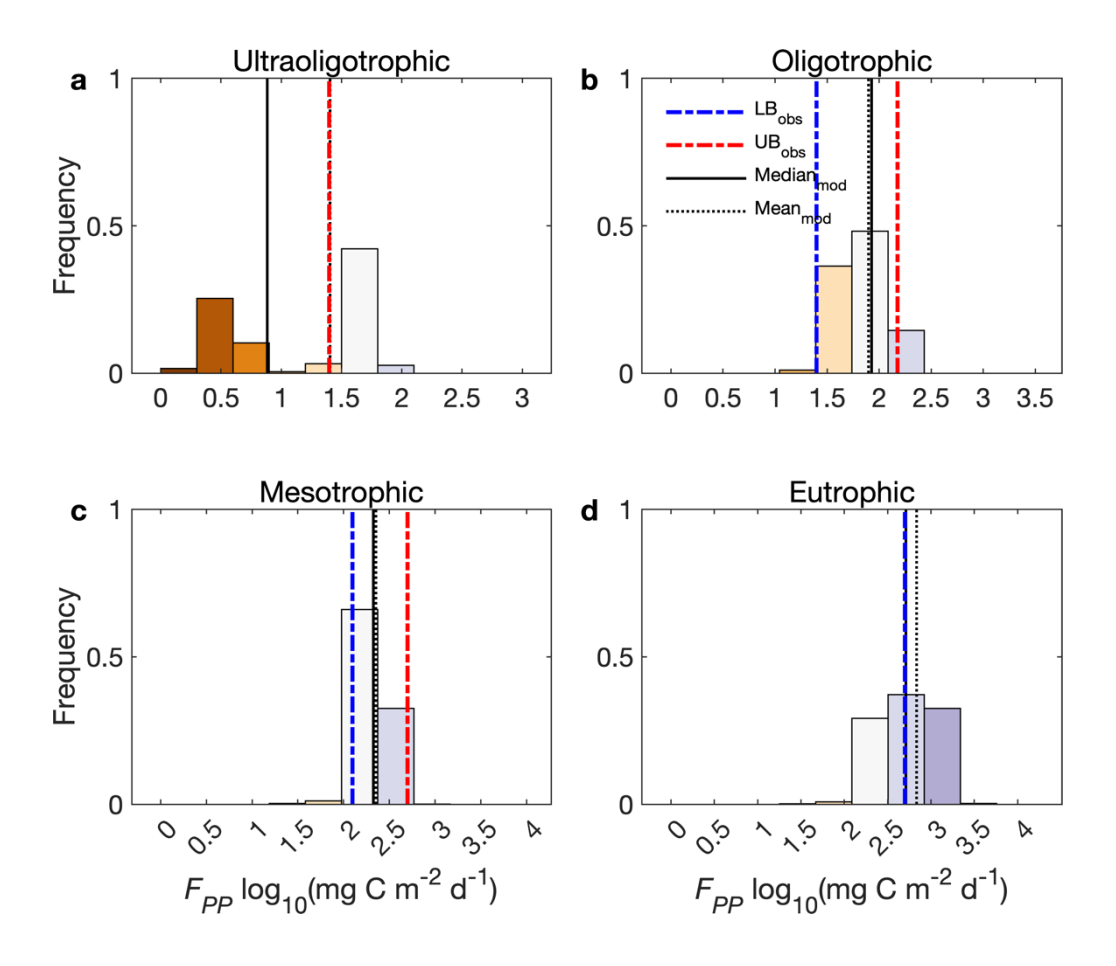


Fig. S19. Comparison of simulated diffusive (top row), ebullitive (middle row) and total (bottom row) CH₄ emission rates (in log scale) with the measurements complied by Rinta *et al.* (2017). The datasets reported by Rinta *et al.* (2017) comprises the diffusive, ebullitive and total emission rates from 17 boreal lakes in Finland and Sweden and 30 lakes of central European lakes in The Netherlands, Germany and Switzerland. The boxes represent the 25% and 75% quartiles, and the whiskers cover the 95% confidence intervals. The same figure with an arithmetic scale is presented in Fig. 7.

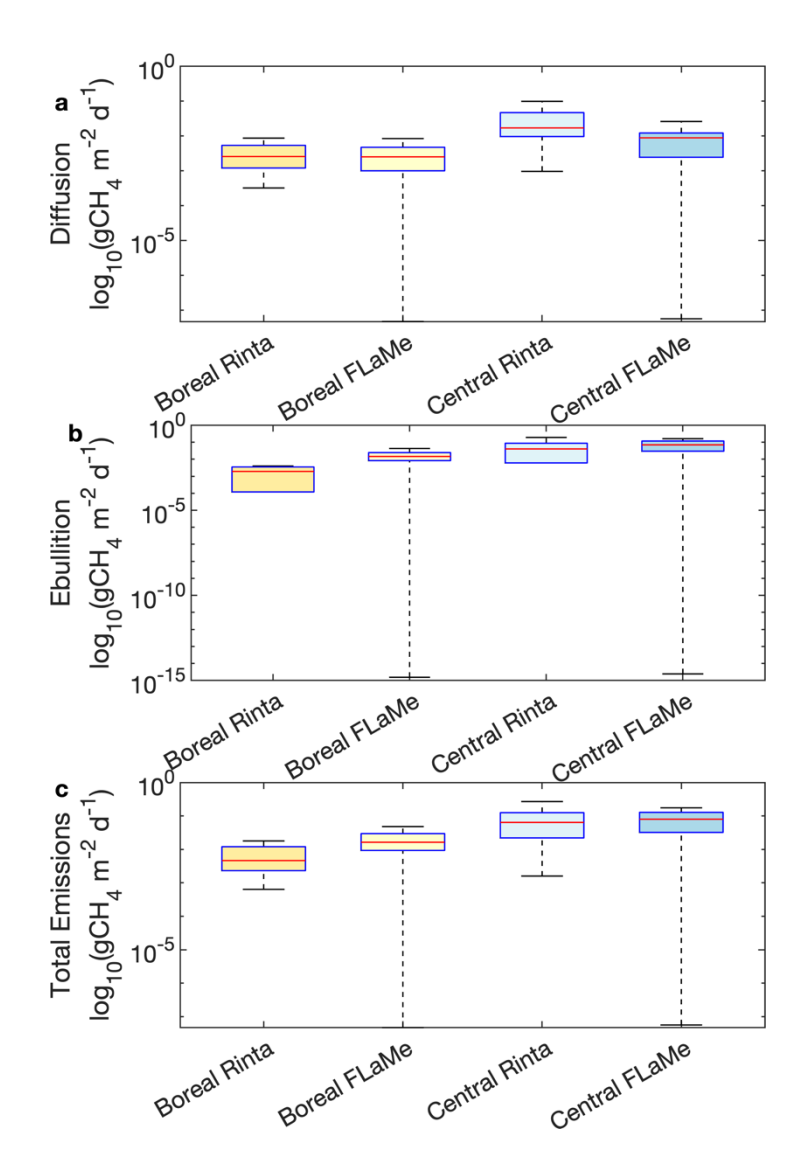


Fig. S20. Comparison of spatial distributions of CH₄ emission rates. (a) CH₄ emission rate (g CH₄ m⁻² yr⁻¹, per *lake* area); (b) CH₄ emission rate (g CH₄ m⁻² yr⁻¹, per *land* area) within each $0.1^{\circ} \times 0.1^{\circ}$ grid cell; (c) aggregated CH₄ fluxes within $0.1^{\circ} \times 0.1^{\circ}$ grid cell (Mg CH₄ yr⁻¹).

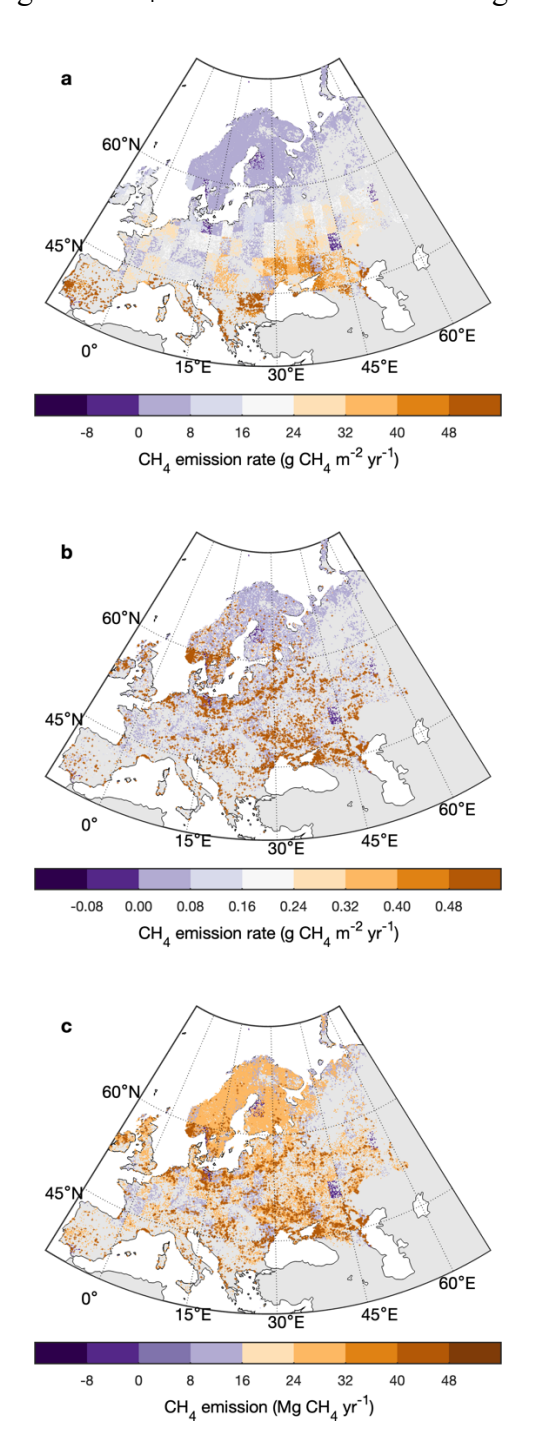


Fig. S21. Comparison of the simulated temperature dependence (θ_s) of net ebullitive methane emissions against observed ranges reported by Aben *et al.* (2017). The histogram shows the frequency distribution of annual mean values of temperature dependence estimated from 953 representative lakes (an annual mean estimate for each lake). The black bold line is the median of our estimates, which falls well within the lower (blue dashed line) and upper (red dashed line) bounds of observed range.

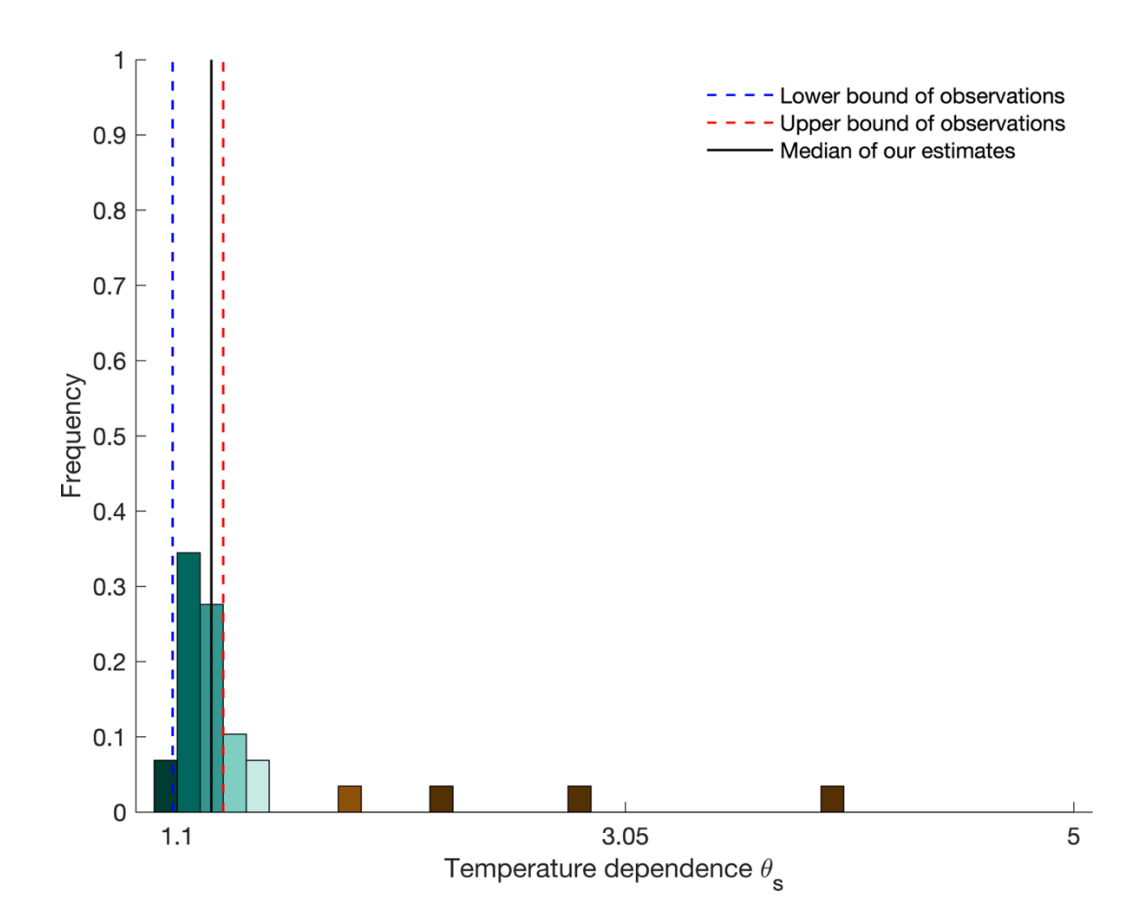


Table S1. The comparison of FLaMe-v1.0 with the existing lake models

	GLM3.0	LAKE2.0	bLake4Me	ALBM	FLaMe-v1.0	
Lake shape	User-specified	Bucket/Valley	Bucket	User- specified/Valley	Valley	
Application	Site	Site/Regional	Site/Global	Site/Global	Regional/Global	
Physical processes						
Water temperature fields	√	V	√	√	√	
Lake stratification & turnover	√	V	√	√	√	
Ice dynamics	√	√	√	√	√	
Sedimentary temperature fields	√	V	√	√	×	
Hydrological routing	√	×	×	×	×	
Biogeochemical processes						
Autochthonous C dynamics	×	V	×	√	√	
P limitation with C	×	×	×	√	√	
N limitation with C	×	×	×	×	×	
Allochthonous C input from thawing	×	V	√	√	×	
Oxygen profile	×	×	×	√	√	
Sedimentary methane production &						
its split between diffusion and	×	\checkmark	\checkmark	\checkmark	\checkmark	
ebullition						
Methane oxidation in water and	×	√	√	J	N	
dissolution in gas bubbles	^	V	V	V	v	
Gas exchanges with air	×			$\sqrt{}$		

a. Red ticks indicate the model has the capability but it was only applied at site level and not to regional or global to scales.

Table S2. Comparison of means and medians (g CH_4 m⁻² d⁻¹) between observed and simulated methane emission rates in boreal and central European lakes. See Fig. 8 and Fig. S19 for a graphical representation.

		Median						
_	Boreal		Central Europe		Boreal		Central Europe	
_	Obs.	Sim.	Obs.	Sim	Obs.	Sim.	Obs.	Sim.
Diffusion	0.0042	0.0029	0.0337	0.0084	0.0026	0.0025	0.0170	0.0088
Ebullition	0.0051	0.0179	0.0846	0.0722	0.0019	0.0146	0.0402	0.0700
Total	0.0089	0.0199	0.1177	0.0807	0.0046	0.0164	0.0642	0.0801